Journal of King Saud University – Engineering Sciences (2018) 30, 345–354

King Saud University

Journal of King Saud University – Engineering Sciences

www.ksu.edu.sa
www.sciencedirect.com

ORIGINAL ARTICLE

Multiphase flow analysis of hydrodynamic journal bearing using CFD coupled Fluid Structure Interaction considering cavitation

D.Y. Dhande [a,*], **D.W. Pande** [b,1]

[a] *Department of Mechanical Engineering, AISSMS College of Engineering, Pune, Maharashtra State 411001, India*
[b] *Department of Mechanical Engineering, College of Engineering, Pune, Maharashtra State 411005, India*

Received 17 June 2016; accepted 26 September 2016
Available online 5 October 2016

KEYWORDS

Multiphase flow;
Journal bearings;
Fluid Structure Interaction;
Cavitation;
CFD;
Optimization

Abstract In this study, a fully three-dimensional CFD analysis and multi-phase flow phenomena, has been successfully implemented for simulation of hydrodynamic journal bearing considering the realistic deformations of the bearing with Fluid Structure Interactions (FSI) along with cavitation. Mixture model is used to model cavitation in the bearing and parametric modelling is used for modifying the flow domain due to deformation. Both systems are coupled and design optimization based on multi objective genetic algorithm (MOGA), is used to obtain optimized solution of the attitude angle and eccentricity for the combination of operating speed and load. In the study of bearings with and without effects of cavitation, it is observed that maximum pressure values drop when cavitation is considered in the bearing. Also there is decrease in maximum pressure when elastic deformation in the bearing is considered. The oil vapour distribution goes on increasing with the increase in shaft speed, thus lowering the magnitude of the pressure build up in the bearing. Multiphase study of bearings with cavitation hence becomes extremely important in case of bearings operating with higher speeds. The experimental data obtained showed very good agreements with numerical results and considerable reduction in computation time is observed.
© 2016 The Authors. Production and hosting by Elsevier B.V. on behalf of King Saud University. This is an open access article under the CC BY-NC-ND license (http://creativecommons.org/licenses/by-nc-nd/4.0/).

1. Introduction

Hydrodynamic journal bearings are widely used due to their simplicity and better damping characteristics in high load, high speed and high precision applications such as gas turbines, electric generators, marine propellers, hydro turbines, IC Engines, hard disk drives and turbo generators. The traditional method for hydrodynamic journal bearing analysis usually applies the lubrication theory based on the Reynolds equation (Brizmer et al., 2003; Buscaglia et al., 2005; D'Agostino and

* Corresponding author at: Department of Mechanical Engineering, AISSMS College of Engineering, 1, Kennedy Road, Pune, Maharashtra State 411001, India.
E-mail addresses: dydhande@aissmscoe.com (D.Y. Dhande), deanr_d@coep.ac.in (D.W. Pande).
[1] Department of Mechanical Engineering, College of Engineering, Shivajinagar, Pune, Maharashtra State 411001, India.
Peer review under responsibility of King Saud University.

Production and hosting by Elsevier

http://dx.doi.org/10.1016/j.jksues.2016.09.001
1018-3639 © 2016 The Authors. Production and hosting by Elsevier B.V. on behalf of King Saud University.
This is an open access article under the CC BY-NC-ND license (http://creativecommons.org/licenses/by-nc-nd/4.0/).

Nomenclature

e	eccentricity between shaft and bearing, m
C	radial clearance, m
R	radius of the shaft, m
h	film thickness, m
ω	angular velocity, rad/s
W	load carrying capacity, N
O'	bearing centre
O	shaft centre
ρ	fluid density, kg/m^3
ρ_l	liquid density, kg/m^3
ρ_v	vapour density, kg/m^3
$\vec{v}$	fluid velocity
P	static pressure, Pa
$\bar{\bar{\tau}}$	stress tensor
$\vec{F}$	external body force, N
t	time
ε	eccentricity ratio
σ	liquid surface tension coefficient
$\vec{v}$	fluid velocity vector
C_e, C_c	mass transfer source terms connected to the growth and collapse of the vapour bubbles respectively
F_{cond}	condensation coefficient
F_{evap}	evaporation coefficient
p_v	saturation pressure of the fluid
$[M_s]$	structural mass matrix
$[M_f]$	fluid mass matrix
$[F_s]$	structural force matrix
$[F_f]$	fluid force matrix
$[R]$	coupling matrix
Δh	relative rigid displacement of the two bearing surfaces
δ	total elastic deformation of the shaft and bearing system
p_b	bubble surface pressure
I	unit tensor
μ	fluid viscosity, Pa-s
R_b	bubble radius, m
a_{nue}	nucleation site volume fraction
p	local pressure
θ	angular coordinate
ϕ	attitude angle
L	length of the bearing

Senatore, 2006) which is a derived form of Navier–Stokes equations (Arghir et al., 2003; Sahlin et al., 2005; Li and Chen, 2007; Wodtke et al., 2013) and continuity equation. This approach has been recognized as very efficient for obtaining fundamental bearing data. Despite its great success, fundamental assumptions made in the basic lubrication theory puts limitations for modelling and simulation of complex flow within realistic bearing geometries Suitable empirical modifications are hence made to cover turbulence, heat transfer, and cavitation. These limitations could be circumvented by applying a computational fluid dynamics (CFD) approach (Chen and Hahn, 1998; Gertzos et al., 2008; Montazeri, 2008) coupled with FSI resting closer to the fundamental physical laws. In hydrodynamic journal bearing analysis using CFD, two simplified approaches are used:

- 2D analysis with cavitation approximation and constant viscosity neglecting viscous heating.
- Approximation of thermal interaction of the film with solid components such as shaft or bearing neglecting elastic deformation in components.

These approaches give approximate solutions that do not meet accurate and detailed performance including elastic deformations and visualization of the realistic flow inside the bearings with complex geometries becomes hard. The commonly used approaches include steady state simulations with free floating shafts and transient simulation for CFD and structural analysis. The first approach does not work, as imbalances in the shaft allow the contact between shaft and bearing, thus perfect force balance is not achieved. Second approach requires a long simulation time to reach equilibrium position. The transient structural analysis coupled to steady state CFD approach works, but is complex and requires artificial damping to stabilize the structural motion. As the speed increases, bearing deformations due to developed hydrodynamic pressure forces increase, modifying the fluid film flow region in the bearing. Hence dynamic remodelling of the geometry becomes a necessity. Moreover, as speed increases a fraction of oil will vaporize, which introduces another phase in the flow. In addition, there is a wider distribution of the vapour in a plain journal bearing that leads to a lower pressure build-up, when compared to a plain bearing without cavitation. This result is different from the solution of the Reynolds equation using the Reynolds boundary condition to determine the onset of cavitation, which results in an increased pressure build-up. Some researchers have worked on analysis of bearings with cavitation coupled with FSI (Wodtke et al., 2013; Lin et al., 2013) and found that the deformations are significant (Jain et al., 1982; Benasciutti and Gallina, 2012). Also, cavitation problem becomes more severe with increase in speed and significant computation time is required (Geller et al., 2014; Riedel et al., 2013; Osman, 2004). Therefore, there is hence a need to develop a platform to compute the performance considering both cavitation and bearing deformation caused by hydrodynamics forces which will also lower computational time. In this present work, Mixture model is used in order to account for cavitation while parametric modelling is used to modify the flow domain as the bearing deforms.

2. Model description

The journal bearing geometry used in the present work is shown in Fig. 1. The bearing centre is represented by O′ and O is the journal or shaft centre, '**e**' is the eccentricity between shaft and bearing centres and '**L**' is the bearing length. The external load '**W**' is assumed as acting vertically along Y axis

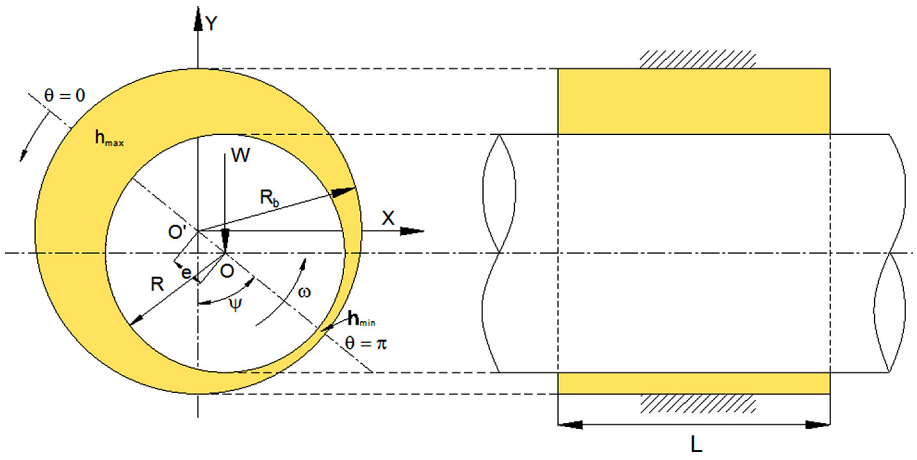

Figure 1 Journal bearing geometry.

and is constant. The hydrodynamic pressure developed in the convergent region, separates the bearing from shaft with a fluid film and balances the external force acting on the shaft. The fluid properties in this region remain constant. As the fluid enters the divergent region, the fluid pressure falls and reaches saturation pressure. In this region, liquid is converted into vapour and as the fluid advances, oil vapour expands and more vapour bubbles are released. This phenomenon is assumed as isothermal expansion and the energy required for the phase change is neglected as the amount of oil vapour formed is small. As the fluid further advances to convergent region, the high pressures react with fluid vapour by diffusion and the vapour is dissolved in the fluid again. This reduces the positive pressure build up in the convergent region.

3. Theory

3.1. Governing equations

The pressure distribution in hydrodynamic journal bearing is governed by Reynolds equation which is derived from Navier Stokes continuity and momentum equations. In FLUENT, these equations are solved for mass and momentum that are valid for all types of flows. The general mass conservation equation for compressible as well as incompressible flow is given as:

$$\frac{\partial \rho}{\partial t} + \Delta(\rho \cdot \vec{v}) = 0 \tag{1}$$

where ρ fluid density, $\vec{v}$ fluid velocity vector.

The momentum equation is:

$$\frac{\partial}{\partial t}(\rho \cdot \vec{v}) + \nabla(\rho \cdot \vec{v} \cdot \vec{v}) = -\nabla P + \nabla(\bar{\bar{\tau}}) + \rho \cdot \vec{g} + \vec{F} \tag{2}$$

where P static pressure, $\bar{\bar{\tau}}$ stress tensor (given in Eq. (3) below), $\rho \cdot \vec{g}$ gravitational force and, $\vec{F}$ external body force.

The stress tensor is written as,

$$\bar{\bar{\tau}} = \mu\left[\left(\nabla \cdot \vec{v} + \nabla \cdot \vec{v}^{T}\right) - \frac{2}{3}\nabla \times \vec{v} \cdot I\right] \tag{3}$$

where,

μ fluid viscosity

I unit tensor, and

The second term on right hand side is effect of volume dilation.

3.2. Cavitation model

In hydrodynamic bearings, shaft rotates eccentrically with bearing forming a convergent and divergent region. In the convergent zone, shaft rotation forces the fluid to pass into an ever decreasing cross-sectional area resulting in an increase in pressures. Conversely, in the divergent region the pressures will decrease to an equal yet negative value as that in the convergent zone. These negative pressures are non-physical and cannot occur in a real fluid. Instead as the pressure begins to drop below atmospheric, the fluid will begin to cavitate and a gaseous phase will begin to fill the divergent region. This gaseous phase can be present in three forms: vaporous, gaseous, or a combination of the two making the flow two-phase (Braun and Hannon, 2010).

This two-phase flow can be solved with a discrete phase model, volume of fluid (VOF) model, mixture model and Eulerian model. The VOF model is mostly used for slug and free surface flows and is not compatible with the cavitation models. Therefore the VOF model is not applicable for simulation of the two-phase flow in a bearing. The discrete phase model is used for flows, wherein the volume fraction of the dispersed-phase does not exceed 10%. The oil-vapour volume fraction becomes higher than 10% in the pressure drop of a bearing. Therefore the discrete phase is also not appropriate for solving the two-phase flow in a bearing. The mixture and Eulerian models are both appropriate for higher volume fraction of the vapour-phase. The Eulerian model is a full multi-phase model; therefore this model is quite expensive with respect to calculation time. Especially in this case, the vapour-phase could have a wide distribution through the bearing. The mixture model is a simplified multi-phase model with almost the same performance as a full multi-phase model, which leads to less expensive calculation times. Therefore the mixture model is used for simulation of the two-phase flow in a bearing in this study.

The mixture model solves the continuity and the momentum equation of the mixture and the volume fraction equation of the vapour-phase. The mass transfer between the phases is needed for these equations. This mass transfer will be solved with a cavitation model using vapour transport equation given below:

$$\frac{\partial}{\partial t}(a_v \cdot \rho_v) + \nabla(a_v \cdot \rho_v \cdot v_v) = C_e - C_C \tag{4}$$

where C_e and C_c account for the mass transfer between liquid and vapour phases in cavitation. They are based on the Rayleigh–Plesset equation describing the growth of a single vapour bubble in a liquid governed by following equation:

$$R_b \cdot \frac{d^2 R_b}{dt^2} + \frac{3}{2}\left(\frac{dR_b}{dt}\right) = \frac{p_b - p}{\rho_l} - \frac{2\sigma}{\rho_l \cdot R_b} - 4 \cdot \frac{\mu_l}{\rho_l \cdot R_b} \cdot \frac{dR_b}{dt} \quad (5)$$

Neglecting the acceleration of the bubble growth and the surface tension (σ), Eq. (5) is simplified to:

$$\frac{dR_b}{dt} = \sqrt{\frac{2}{3} \cdot \frac{p_b - p}{\rho_l}} \quad (6)$$

This equation provides a physical approach to introduce the effects of bubble dynamics into the cavitation model. It can also be considered to be an equation for void propagation and hence mixture density. A Rayleigh–Passet based cavitation model is fully integrated in the CFD package ANSYS CFD (ANSYS Inc. ANSYS® CFD 16.0) viz Singhal model (Singhal et al., 2002) and Zwart-Gerber–Belamari model (Zwart et al., 2004). The Singhal model takes non-condensable gasses into account, therefore this model is numerically less stable in comparison to the other model. Hence, in the present work, Zwart–Gerber–Balamri model is used due to its precise prediction performance and good convergence behaviour. The final form of this cavitation model is as follows:

If, $p < p_v$

$$C_e = F_{evap} \cdot \frac{3 \cdot a_{nue}(1 - a_v) \cdot \rho_v}{R_b} \cdot \sqrt{\frac{2}{3} \cdot \frac{p_v - p}{\rho_l}} \quad (7)$$

If $p \geqslant p_v$

$$C_C = F_{cond} \frac{3 \cdot a_v \cdot \rho_v}{R_b} \cdot \sqrt{\frac{2}{3} \cdot \frac{p - p_v}{\rho_l}} \quad (8)$$

R_b bubble radius $= 10^{-6}$ m, a_{nue} nucleation site volume fraction $= 5 \times 10^{-4}$, F_{evap} evaporation coefficient $= 50$, F_{cond} condensation coefficient $= 0.01$.

3.3. Fluid Structure Interaction (FSI)

The fluid and the bearing affect each other. Fluid flow exerts a pressure on the bearing causing it to deform thus modifying the flow domain. The static structural capability of ANSYS is used to find deformations in the bearing. The governing equations are:

$$[M_s]\{\ddot{U}\} + [K_s] \cdot \{U\} = [F_s] + [R] \cdot \{P\} \quad (9)$$

$$\begin{bmatrix} M_s & 0 \\ \rho R^T & M_f \end{bmatrix} \cdot \begin{Bmatrix} \ddot{U} \\ \ddot{P} \end{Bmatrix} + \begin{bmatrix} K_s & R \\ 0 & K_f \end{bmatrix} \cdot \begin{Bmatrix} U \\ P \end{Bmatrix} = \frac{F_s}{F_f} \quad (10)$$

where $[M_s]$ is the structural mass matrix; $[M_f]$ is the fluid mass matrix; $[F_s]$ and $[F_f]$ is the structural and fluid force matrix; $[R]$ is a coupling matrix that represents the effective surface area associated with each node in fluid structure interface.

3.4. Lubricant film thickness

The relative displacement of the Fluid–Structure interfaces in the fluid domain is consistent with that of the solid domain. The film thickness is defined as the distance between the rotor-lubricant interface and the bearing-lubricant interface, including both rigid and elastic deformations between the two bearing surfaces as:

$$h = C + \Delta h + \delta \quad (11)$$

where h film thickness, C radial clearance of the bearing system, Δh relative rigid displacement of the two bearing surfaces and δ total elastic deformation of the two bearing surfaces.

3.5. Assumptions and boundary conditions

The Navier Stokes equations are solved using 3D double precision pressure based steady state analysis. As the Reynolds number is very low, laminar and isothermal flow conditions are assumed. The fluid domain, shown in Fig. 2(a) is meshed using hexahedral elements in CFD. The lubricant film is provided with 4 layers in radial direction. Element size of 0.6 mm is used giving total number of elements 102,636. The solid domain, shaft and bearing shown in Fig. 2(b) are meshed using tetrahedral meshing with 184,145 elements. The lubricant supply hole is specified as 'pressure inlet' and the sides of the lubricant are specified as 'pressure outlet' with gauge pressure as zero. The inlet pressure is taken as 101.325 kPa. The bearing is modelled as 'stationary wall' and the shaft is modelled as 'moving wall' with absolute rotation speed. Initially the shaft axis position is defined by an arbitrary value of eccentricity and the attitude angle, and these values are given as input to shaft rotation axis origin. To model the change in thickness of fluid domain, dynamic mesh technique in FLUENT is used. The mesh is then transferred to fluent for flow analysis. The smoothing mesh method is used with a convergence tolerance of 10E−6 and number of iterations are 50.

3.6. Design explorer approach

The method is based on the finding out the equilibrium position of the shaft where there is a force balance between the shaft load and fluid reaction forces at constant speed and constant shaft load. At equilibrium position, the fluid forces in vertical direction (X-load here) balance the shaft load (W) and the fluid forces in horizontal direction (Y-imbalance) are zero. Initially, for given load and speed, the shaft rotation axis is fixed at predefined position in terms of eccentricity and attitude angle in parametric form and the system is solved to get fluid forces in X and Y directions. The fluid forces are computed in computational fluid dynamics (CFD) domain and structural deformations are computed in structural domain. These two systems are system coupled to perform elastohydrodynamics. The fluid forces developed in CFD are transferred to structural domain and vice versa. Then design optimization is carried out to find equilibrium position of the shaft. Initially, since the shaft rotation axis is fixed i.e.as it is not allowed to float, perfect balance in X and Y directions is not achieved. Hence design exploration cannot be used to get response surface with different shaft positions and equilibrium position. Fig. 3 gives details of response surface showing shaft positions in terms of eccentricity verses X-direction fluid reaction force while Fig. 4 shows shaft position versus Y direction fluid reaction force. The objective is to find point on this response sur-

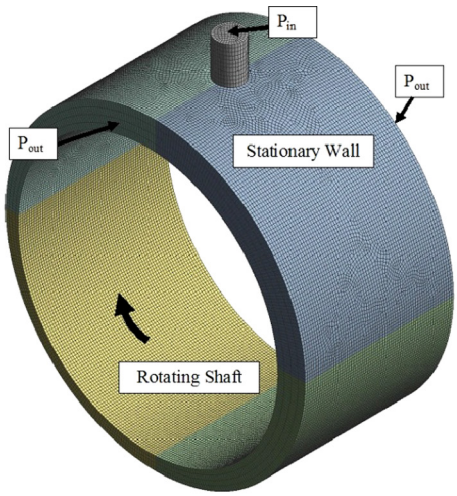

(a) Geometry and mesh of fluid Domain: Oil Film

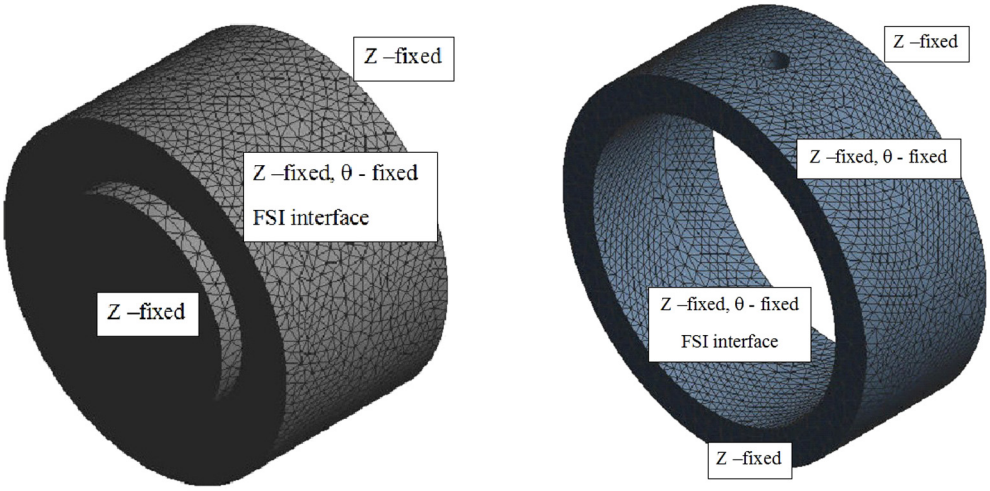

(b) Geometry and mesh of solid Domain : Journal and Bearing

Figure 2 Three dimensional finite element representation of journal bearing system.

face where *Y* imbalance is zero and fluid reaction force in *X*-direction balances the shaft load. Therefore the problem is transformed into optimization with the targets to seek the *Y*-imbalance zero and *X*-load equal to shaft load giving correct equilibrium position of the shaft.

The design exploration has three stages viz. Design of experiments (DOE), Response Surface Analysis (RSA) and Optimization. DOE is used to determine set of eccentricities and attitude angles that are used to build response surface. The values for upper and lower bounds of the eccentricity and attitude angle are specified within which the solution is expected. An optimal space filling design algorithm is used to get design points and matrix of experiments is generated. These design points are used to build response surface which analyses the relationship between eccentricity, attitude angle and output parameters (fluid reaction forces).

The goodness of fit shown in Fig. 5 is observed to see how well the surface fits close to the data points. The response surfaces are examined to get the values of potential solutions which satisfy the optimization criteria. The optimization is based on response surface evaluation. Multi Objective Genetic Algorithm (MOGA), which is based on controlled elitism concepts with non-parametric regression analysis, is used. It supports multiple objectives and constraints to find the global optimum solution. To get the more close solution, more refinement design points are added to the solution and the process is repeated till the optimum equilibrium position of shaft is achieved.

The dimensions and the properties of the materials used in this study are listed in Table 1.

4. Experimental setup

Experimental setup consists of a shaft of 50 mm diameter supported in two self aligned bearings and bearing to be tested

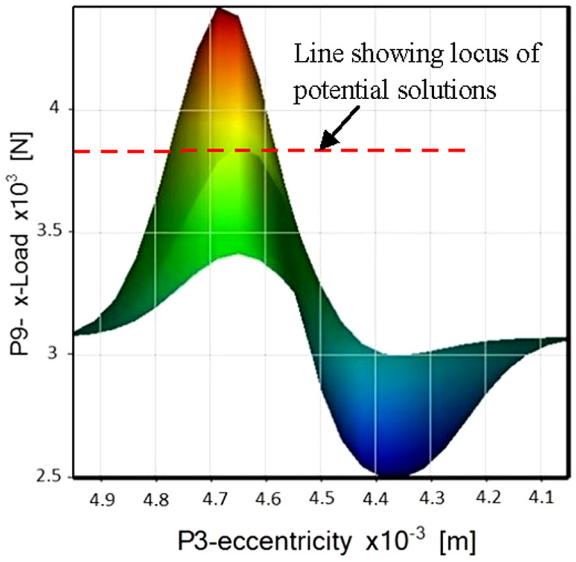

Figure 3 Response surface for vertical load.

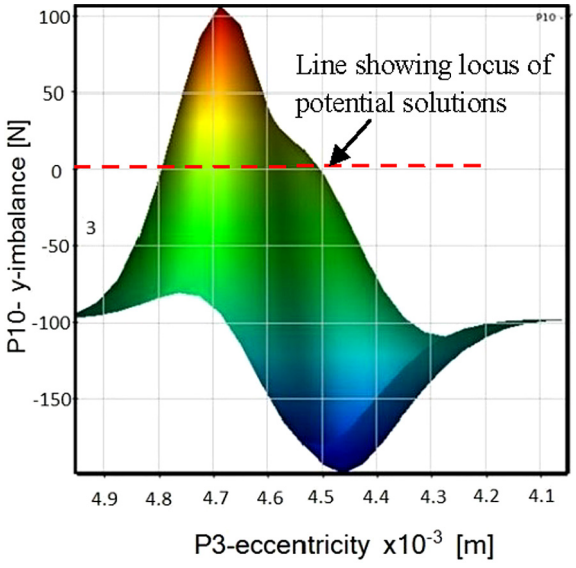

Figure 4 Response surface of horizontal (X) imbalance.

floats on the shaft as shown in Fig. 6(a). The shaft is driven with the help of a drive motor and the speed of the motor is controlled with the help of variable frequency drive. A pulley setup is designed to step up the speed of the motor from its rated speed. The bearing is loaded with the help of belt and the loading is sensed with S type strain gauge load cell of capacity 1000 N ($\pm$100 g). There are nine pressure sensors mounted at the mid-plane of the bearing circumferentially to measure circumferential pressures in the loaded zone as shown in Fig. 6(b). Digital indicator is used to record the pressure readings and the location can be changed using multipoint indicator switch. The eccentricity is measured with the help of proximity sensor mounted on bearing housing and connected to data acquisition system for recording. The test oil used is supplied through an inlet supply system consisting of

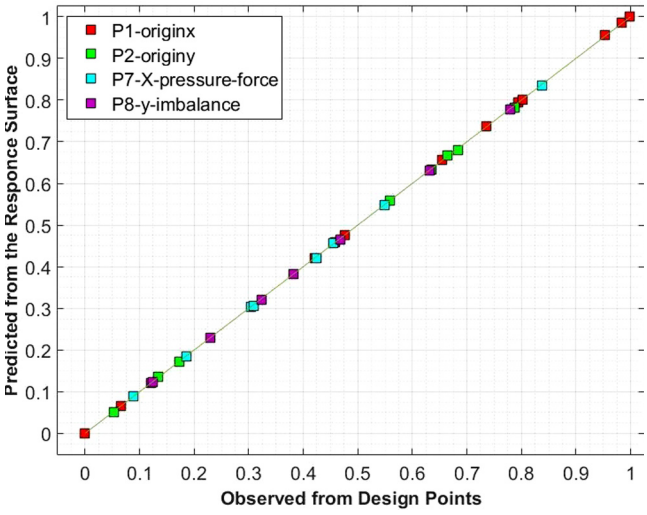

Figure 5 Goodness of fit curve.

Table 1 Parameters used in analysis.

Parameter	Value
Shaft diameter, D	50 mm
Clearance, C	50 μm
Length of the bearing, L	25 mm
Speed, N	1000, 2000, 3000, 4000, 5000 RPM
Lubricant Viscosity, μ	0.0125 Pa-s
Lubricant density, ρ	850 kg/m^3
Oil vapour saturation pressure	29,185 Pa
Oil vapour dynamic viscosity	2×10^{-5}
Material:	
Shaft: steel	Elastic modulus = 210 GPa Density, ρ_s = 7850 kg/m^3 Poison ratio = 0.3
Bearing: aluminium	Elastic modulus = 210 GPa Density, ρ_A = 2700 kg-m^3 Poison ratio = 0.334

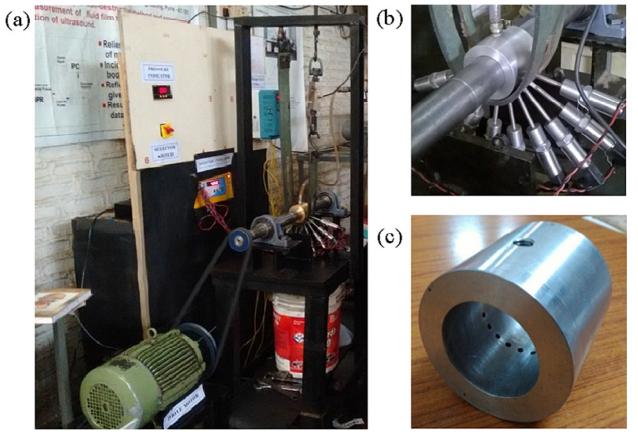

Figure 6 (a) Test setup; (b) pressure sensor arrangement and (c) test bearing.

gear pump at a constant pressure. The test bearing is shown in Fig. 6(c).

The tests are carried out for a speed ranging from 1000 to 5000 RPM. The loading is provided with the help of belt arrangement. The desired speed is set with the help of variable frequency drive. The system is allowed to achieve a steady state for half an hour and corresponding pressures and eccentricities are measured. Three sets of the readings were taken for each speed and the average reading is taken for the analysis. The experimental results are plotted and compared with the numerical results.

5. Results and discussion

5.1. Validation study

The numerical case was developed using proposed approach and the numerical results in published data represented in references (Guo et al., 2005) were compared. The lubricant supply pressure was 101,325 Pa, rotational speed was 10,000 RPM and 25 μ film thickness was assumed. The value of attitude angle and load carrying capacity is predicted neglecting elastohydrodynamic as well as cavitation effects. The proposed numerical method gives a value of an attitude angle of 52.23°, load carrying capacity of 1160. 38 N and maximum pressure 2.1523 MPa at eccentricity of 25.19 μ as compared to 49.8°, 1160 N and 2.31 MPa at 25 μ eccentricity given by Guo et al. This is acceptable since cavitation as well as elastohydrodynaimic effect reduce the maximum pressure developed in the convergent region. This validates the proposed numerical method.

5.2. Effect of cavitation

The numerical results are given for the journal bearing when the journal bearing is loaded and the shaft is eccentric to the bearing position which generates positive pressure to support external load applied. Fig. 7(a) shows pressure built up and pressure drop in a journal bearing and in Fig. 7(b), the pressure distribution is changed to a pressure build up and the pressure drop has disappeared due to cavitation. The pressure build up lies closer to the smallest gap and ends behind the smallest gap that leads to a different reaction on the shaft. This corresponds with the Reynolds boundary condition which states that the gradient of the pressure over the angle should be zero.

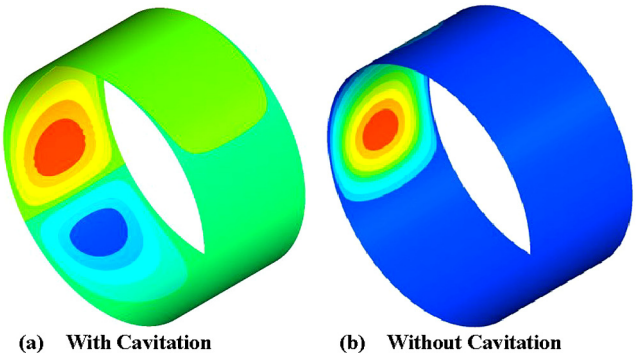

Figure 7 Pressure contours generated for journal bearing.

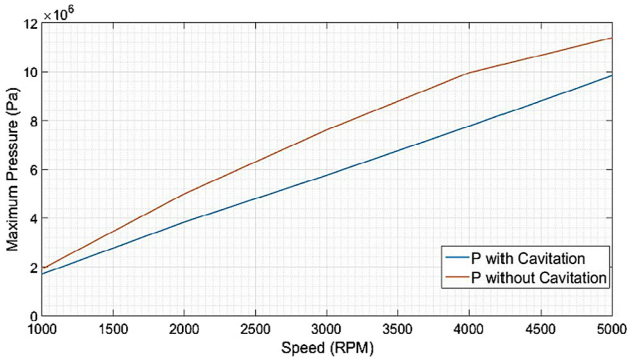

Figure 8 Comparison of maximum pressures in journal bearing with and without cavitation.

The comparison of maximum pressure developed for bearing with and without cavitation is presented in Fig. 8 at various operating speeds. The magnitude of the pressure build up is also changed, which is slightly lower than the pressure build up without cavitation.

The comparison of the circumferential pressure distribution in convergent zone is shown in Fig. 9 for both bearings, which indicates that the peak pressure in journal bearing without cavitation is more than that of with cavitation. This confirms the fact that the cavitation lowers the peak value of the positive pressure build up.

5.3. Elastohydrodynamic effect

Fig. 10 shows the comparison between numerical pressure distribution with rigid (Boyd and Raimondi assumption) and with elastohydrodynamics consideration. It is evident that the peak pressure value drops when elastic deformations are considered as compared with rigid maximum pressure value. Due to elastic deformation in the bearing, the clearance space between shaft and bearing increases which allows more lubricant to fill in the space reducing the maximum pressure generated as compared to rigid assumption.

5.4. Effect of rotational speed and eccentricity ratio

Fig. 11 shows the comparison between numerical results and experimental data for pressure distribution on the mid plane of the shaft for various eccentricity ratios (ε). It is observed that the peak pressure goes on increasing with increase in eccentricity ratio (ε). The peaks are low for lower eccentricity ratio (ε) values, but are significant when eccentricity ratios (ε) are 0.8 and 0.9. Also the range of peak pressure becomes narrow at these two values. When eccentricity ratio (ε) is in the range of 0.2–0.6, the peak pressure value is too low to separate the journal and bearing.

Fig. 12 shows the comparison between numerical results and experimental results for pressure distribution for eccentricity ratio (ε) 0.8 at various rotational speeds of shaft. The peak pressure increases with increase in rotational speed of the shaft but the range of peak pressure goes on gradually reducing as compared to the peak pressure range in case of eccentricity

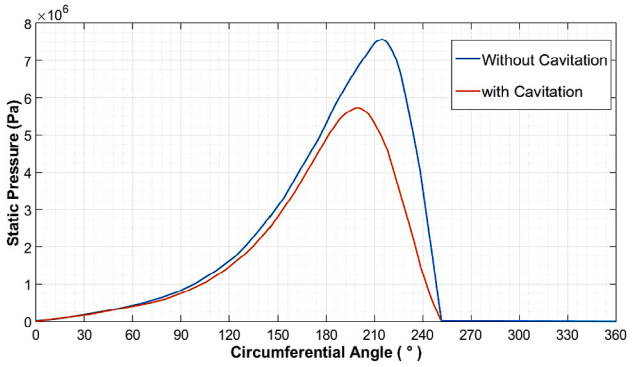

Figure 9 Comparison of circumferential pressure distribution in journal bearing with and without cavitation.

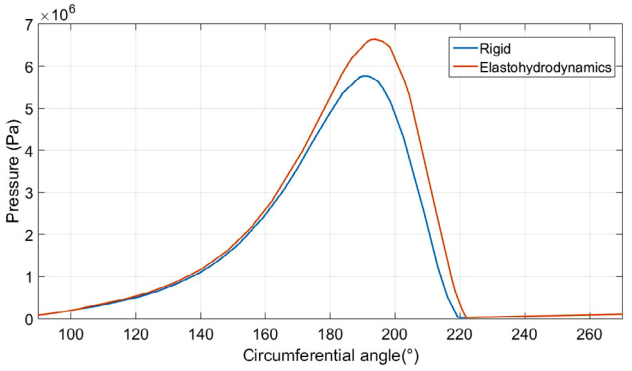

Figure 10 Comparison of circumferential pressure distribution in journal bearing with rigid and elastohydrodynamics assumption.

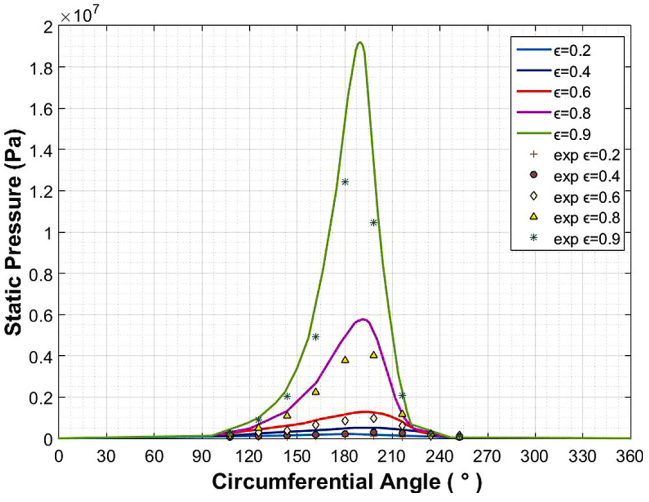

Figure 11 Comparison of circumferential pressure distribution for CFD model and experimental data at various eccentricity ratios (N = 3000 RPM).

ratio (ε). Also for eccentricity ratio 0.8 to 0.9, there is steep rise in peak pressure at constant speed (N = 1000 RPM) whereas in case of constant eccentricity ratio (ε = 0.8), pressure goes on increasing gradually.

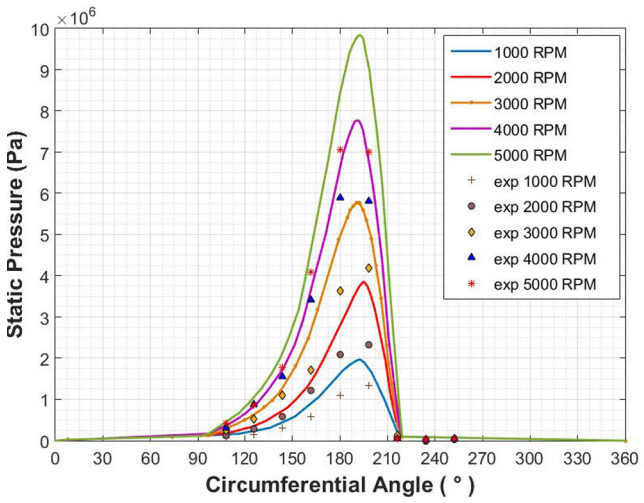

Figure 12 Comparison of circumferential pressure distribution for CFD model and experimental data at various shaft speeds for ε = 0.8.

5.5. Effect of rotational speed on vapour volume fraction

Fig. 13 shows the volume fraction of the oil vapour (%) in the journal bearing for eccentricity ratio 0.8 and for various speeds. It is observed that the distribution of the oil vapour goes on increasing with increase in speed of rotation of shaft. This is significant since it is assumed that after the inlet, all the oil vapour bubbles are expelled. It can be explained with the increase in rotational speed of the shaft. The shaft drags more and more oil vapour bubbles into inlet tube where new liquid oil enters the journal bearing. This new liquid oil does not have the force to expel the oil vapour bubbles since it is also dragged by fast rotating shaft. When the film is converging, the liquid oil is squeezed and pushes the oil vapour bubbles out of the journal bearing. It also explains the lower magnitude of the pressure build up, because the pressure build up will appear only in liquid oil. The pressure build up, hence cannot increase as much as in the journal bearing without cavitation. The remaining oil in the cavitation area is thrown against the housing of the journal bearing and the oil vapour bubbles stay closer to the shaft, which is caused due to difference in density. The remaining oil in the convergent region is thrown out by the centrifugal force due to speed of the shaft, which would suggest that velocity slip between the oil and the oil vapour bubbles appears in a journal bearing while the velocity slip is not considered in the cavitation model. The pressure build up is not sufficiently lower when velocity slip is considered in the cavitation model. The velocity slip between the oil and oil vapour bubbles is hence neglected for the simulations with cavitation.

6. Conclusions

This research work studies hydrodynamic journal bearing with multiphase flow. A new numerical method comprising CFD and FSI methodology with optimization is proposed where both inertial as well as cavitation effects are considered. The experimental data obtained provide very good concordance

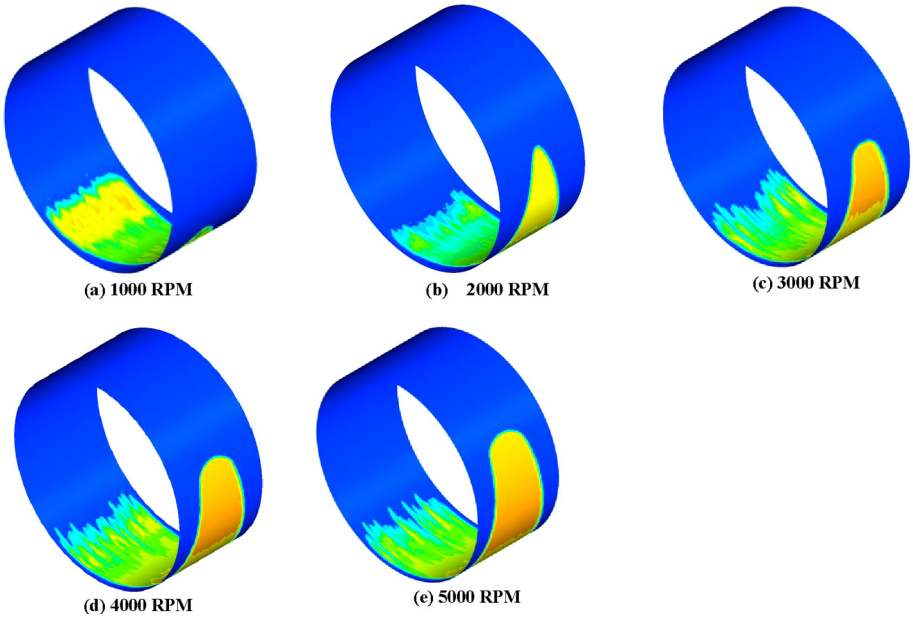

Figure 13 Vapour volume fraction of oil vapour (%) in journal bearing for $\varepsilon = 0.8$.

with numerical results. The following conclusions can be made:

1. The magnitude of the pressure build up lowers as compared to the pressure build up in journal bearings without cavitation. The oil vapour distribution in the bearing goes on increasing with increase in the shaft rotational speeds thus lowering the value of the pressure build up. The multiphase flow analysis with cavitation hence is extremely important in case of the bearings operating with higher speeds.
2. The peak pressure increases with increase in both shaft speed as well as eccentricity ratio but more sensitive to eccentricity ratio change, thus making the situation tightly coupled.
3. The peak pressure value drop when elastohydrodynamic effect is considered.
4. The design optimization approach presented here provides the platform for accurate performance of the bearings by considering the realistic flow conditions as well as deformations in the bearing due to hydrodynamic forces developed in the bearing.
5. The computation time is also significantly reduced by this approach.

Funding

This research did not receive any specific grant from funding agencies in the public, commercial, or not-for-profit sectors.

References

Arghir, M., Roucou, N., Helene, M., Frene, J., 2003. Theoretical analysis of the incompressible laminar flow in a macro-roughness cell. J. Tribol. 125, 309. http://dx.doi.org/10.1115/1.1506328.

Benasciutti, D., Gallina, M., 2012. A numerical approach for the analysis of deformable journal bearings. Fract. Struct. 21, 37–45. http://dx.doi.org/10.3221/IGF-ESIS.21.05.

Braun, M.J., Hannon, W.M., 2010. Cavitation formation and modelling for fluid film bearings: a review. Proc. Inst. Mech. Eng. Part J J. Eng. Tribol. 224, 839–863. http://dx.doi.org/10.1243/13506501JET772.

Brizmer, V., Kligerman, Y., Etsion, I., 2003. A laser surface textured parallel thrust bearing. Tribol. Trans. 46, 397–403. http://dx.doi.org/10.1080/05698190490426007.

Buscaglia, G.C., Ciuperca, I., Jai, M., 2005. The effect of periodic textures on the static characteristics of thrust bearings. J. Tribol. 127, 899. http://dx.doi.org/10.1115/1.2033896.

Chen, P.Y.P., Hahn, E.J., 1998. Use of computational fluid dynamics in hydrodynamic lubrication. Proc. Inst. Mech. Eng. Part J J. Eng. Tribol. 212 (6), 427–436. http://dx.doi.org/10.1243/1350650981542236.

D'Agostino, V., Senatore, A., 2006. Analytical solution for two-dimensional Reynolds equation for porous journal bearings. Ind. Lubr. Tribol. 58, 110–117. http://dx.doi.org/10.1108/00368790610651521.

Geller, M., Schemmann, C., Kluck, N., 2014. Simulation of radial journal bearings using the FSI approach and a multi-phase model with integrated cavitation. Prog. Comput. Fluid Dyn. 14, 14–23.

Gertzos, K.P., Nikolakopoulos, P.G., Papadopoulos, C.A., 2008. CFD analysis of journal bearing hydrodynamic lubrication by Bingham lubricant. Tribol. Int. 41, 1190–1204. http://dx.doi.org/10.1016/j.triboint.2008.03.002.

Guo, Z., Hirano, T., Kirk, R.G., 2005. Application of CFD analysis for rotating machinery—Part I: hydrodynamic, hydrostatic bearings and squeeze film damper. J. Eng. Gas Turbines Power 127, 445. http://dx.doi.org/10.1115/1.1807415.

Jain, S.C., Sinhasan, R., Singh, D.V., 1982. Elastohydrodynamic analysis of a cylindrical journal bearing with a flexible bearing shell. Wear 78, 325–335. http://dx.doi.org/10.1016/0043-1648(82)90243-5.

Li, J., Chen, H., 2007. Evaluation on applicability of reynolds equation for squared transverse roughness compared to CFD. J. Tribol. 129, 963. http://dx.doi.org/10.1115/1.2768619.

Lin, Q., Wei, Z., Wang, N., Chen, W., 2013. Analysis on the lubrication performances of journal bearing system using compu-

tational fluid dynamics and fluid–structure interaction considering thermal influence and cavitation. Tribol. Int. 64, 8–15. http://dx.doi.org/10.1016/j.triboint.2013.03.001.

Montazeri, H., 2008. Numerical analysis of hydrodynamic journal bearings lubricated with ferrofluid. Proc. Inst. Mech. Eng. Part J J. Eng. Tribol. 222, 51–60. http://dx.doi.org/10.1243/13506501jet314.

Osman, T.A., 2004. Effect of lubricant non-Newtonian behavior and elastic deformation on the dynamic performance of finite journal plastic bearings. Tribol. Lett. 17, 31–40. http://dx.doi.org/10.1023/B:TRIL.0000017416.95176.30.

Riedel, M., Schmidt, M., Stücke, P., 2013. Numerical investigation of cavitation flow in journal bearing geometry. EPJ Web Conf. 45, 01081. http://dx.doi.org/10.1051/epjconf/20134501081.

Sahlin, F., Glavatskih, S.B., Almqvist, T., Larsson, R., 2005. Two-dimensional CFD-analysis of micro-patterned surfaces in hydrodynamic lubrication. J. Tribol. Asme 127, 96–102. Doi 10.1115/1.1828067.

Singhal, A.K., Athavale, M.M., Li, H., Jiang, Y., 2002. Mathematical basis and validation of the full cavitation model. J. Fluids Eng. 124, 617. http://dx.doi.org/10.1115/1.1486223.

Wodtke, M., Olszewski, A., Wasilczuk, M., 2013. Application of the fluid–structure interaction technique for the analysis of hydrodynamic lubrication problems. Proc. Inst. Mech. Eng. Part J J. Eng. Tribol. 227, 888–897. http://dx.doi.org/10.1177/1350650113481147.

Zwart, P., Gerber, A., Belamri, T., 2004. A two-phase flow model for predicting cavitation dynamics. In: Fifth Int. Conf. Multiph. Flow, Yokohama, Japan, May 30–June 3.